This manuscript was accepted by Phys. Fluids. Click here to see the version of record.

Marginally turbulent Couette flow in a spanwise confined passage of square cross-section

Bayode E. Owolabi[1, 2] and Chao-An Lin[1, a)]

[1)] *Department of Power Mechanical Engineering, National Tsing Hua University, Hsinchu 30013, Taiwan*

[2)] *School of Engineering, University of Liverpool, Liverpool, L69 3GH, UK*

(Dated: 13 June 2018)

The results of direct numerical simulations to determine the critical conditions for self-sustained turbulence in wall-driven (Couette) square duct flow and its characteristics at relatively low turbulent Reynolds numbers are presented. We focus on the case in which a pair of opposite counter-moving walls translating with the same speed drive the flow. Stabilisation by the side walls is found to play a crucial role in the transition to turbulence, the minimum Reynolds number for maintaining a turbulent state ($Re_c \approx 875$) being much greater than that in a plane channel. At Reynolds numbers close to the critical, an alternation of the flow field, in time, between two states characterised by a four-vortex secondary flow pattern is observed, one being a mirror reflection of the other, and the flow remaining approximately symmetrical about the common bisector of the moving walls. Due to the intermittency, large velocity fluctuations about the long-term mean are observed at different locations in the duct. These findings are consistent with results of previous studies on turbulent pressure-driven (Poiseuille) square duct flow at low Reynolds numbers, hence the phenomenon is not unique to Poiseuille flows. Instantaneous flow field visualisations reveal the existence of coherent structures which are persistent over the length of the duct, thus indicating that the states are very stable in the streamwise direction. Quadrant analysis of the Reynolds shear stress show that the secondary motions are closely related to the near-wall ejection and sweeping events.

[a)] Electronic mail: calin@pme.nthu.edu.tw

I. INTRODUCTION

Turbulent flow in a straight square duct is known to be characterised by a mean secondary motion in the cross sectional plane referred to as Prandtl's secondary flow of the second kind. This phenomenon, induced by the turbulent fluctuations was first observed by Nikuradse[1] and has since been widely researched, both experimentally and numerically, to better understand the origin. Earlier experimental studies[2–4] focused on relatively large Reynolds numbers ($Re_\tau > 4000$, $Re_\tau = u_\tau h/\nu$, where u_τ is the friction velocity given by the expression: $\sqrt{\tau^*/\rho}$ and τ^*, h, ν and ρ represent the average shear stress at the wall centre, duct half-height, kinematic viscosity and density, respectively). Although typically less than 2% of the primary flow, the secondary currents characterised by eight vortices which are symmetrical about both the corner and wall bisectors were shown to significantly influence momentum and heat transport. Hence they are of great importance in a wide range of engineering applications such as heating ventilation and air-conditioning systems, nuclear reactor channels, intake ducts of jet engines, heat exchangers and turbine blade cooling passages among others.[5] The sense of rotation of the secondary vortices in a purely pressure-driven flow is such that they are directed towards the corners along the duct's diagonals, resulting in the deformation of the primary velocity profile and a non-uniform wall shear stress distribution. These findings have been confirmed by direct numerical simulations (DNS),[6–9] albeit at much lower Reynolds numbers($Re_\tau < 600$), and detailed flow field statistics not easily obtainable in the laboratory are now available.

In recent times, there has been a growing interest in understanding the flow structure at Reynolds numbers close to transition. In this regime where the separation between small and large scales is small, the duct's width in wall units is just barely large enough to host the minimum number of structures required for self-sustained turbulence.[10,11] The DNS of Uhlmann *et al.*[10] in marginally-turbulent flow revealed a temporal switching of the flow field between two states characterised by a four-vortex mean secondary flow pattern, one state being a 90° rotation of the other about the duct's axis, so that a long time average resulted in the well-known eight vortex pattern in pressure driven flow. These results have been validated by experiments.[12] The probability density functions (p.d.f.s) of streamwise velocity as well as joint p.d.f.s of streamwise and wall-normal velocity at certain distances from the wall were observed to feature two peaks corresponding to each of the two states.

While there has been several studies on the pressure-driven (Poiseuille) case, wall-driven (Couette) turbulent flow in a square duct remains largely unexplored. Large eddy simulations of Couette-Poiseuille flow by Hsu *et al.*[13] and Lo and Lin[14] revealed significant changes to the secondary flow in the vicinity of a moving wall. As the ratio of the wall to bulk velocity increased, a merger of the secondary vortices was observed and the cross-stream flow changed from the eight-vortex pattern to one characterised by six vortices, with symmetry only about the moving-wall bisector. A similar secondary flow pattern was observed in the purely wall-driven case, but the flow was not examined in detail. The Reynolds number in the aforementioned numerical studies on square duct Couette flow are quite high ($Re_\tau > 300$), hence the flow characteristics close to transition are not well known. An interesting question is whether the switching observed in the pressure driven case also exists in wall-driven flow.

In this study, we investigate the purely wall-driven turbulent flow in a square duct using direct numerical simulations. First, we determine the critical conditions for self-sustained turbulence. Motivated by the findings of Uhlmann *et al.*[10] on the existence of bi-stable states in "marginally turbulent" Poiseuille square duct flows, we then characterise the turbulence field at relatively low Reynolds numbers with a view to determining whether this phenomenon is a ubiquitous feature of wall-bounded flows. For a mean secondary flow to exist, a duct of finite aspect ratio is required. In this regard, a square duct is the simplest and most widely studied geometry, thus it was selected to allow for direct comparison with results on pressure-driven flow[10]. We focus on the case in which a pair of opposite counter-moving walls translating with the same speed (U_w) drive the flow. This configuration results in a zero net transport of fluid through the duct.

II. NUMERICAL METHOD

We consider turbulent Couette flow of an incompressible Newtonian fluid through a straight duct of square cross-section ($2h \times 2h$). The streamwise direction is x while y and z are the transverse and spanwise directions, respectively, with u, v and w being the corresponding velocity components. An illustration of the computational domain is shown in Fig. 1. The governing equations for this flow are those expressing the conservation of mass and momentum, which in tensor notation, are given as:

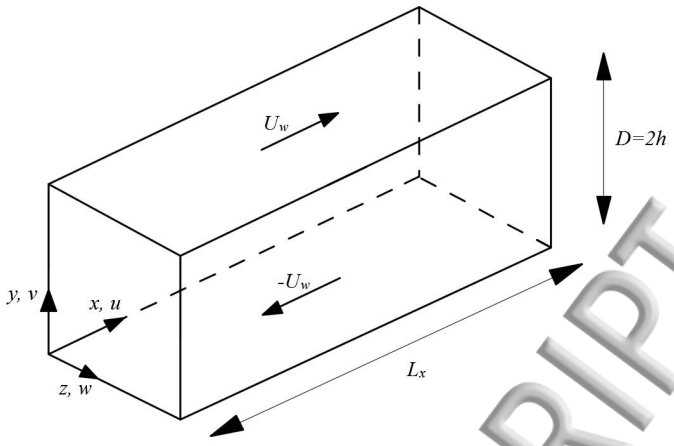

FIG. 1. Coordinate system and geometry

$$\frac{\partial u_i}{\partial x_i} = 0 \tag{1}$$

$$\frac{\partial u_i}{\partial t} + u_j \frac{\partial u_i}{\partial x_j} = -\frac{1}{\rho}\frac{\partial p}{\partial x_i} + \nu \frac{\partial^2 u_i}{\partial x_j^2}, \tag{2}$$

where u_i, p and t denote the velocity field, static pressure and time, respectively, and the mean pressure gradient in the streamwise direction is equal to zero. The boundary conditions employed are the no-slip conditions at the walls and periodicity in the streamwise direction. In solving the Navier-Stokes equations, the finite volume approach is employed. The equations are advanced in time using a semi-implicit fractional step method. The convection and diffusion terms are evaluated by the Adams-Bashforth and Crank-Nicholson schemes, respectively, while spatial derivatives are approximated using second-order central difference schemes. The resulting system of algebraic equations are evaluated using the preconditioned conjugate gradient solver. A Poisson equation for pressure is solved at each time step to obtain the incompressible velocity field. The three dimensional Poisson equation is reduced, using fast Fourier transform, to uncoupled two-dimensional algebraic equations which are solved by LU decomposition.

The code used in this study is a modified version of that employed by Hsu *et al.*[13] and Lo and lin[14] and has been validated against turbulent Poiseuille flow data. Symmetrically clustered grids were employed in the cross-sectional plane, the spacing increasing with distance from the wall. Along the bisector of the moving walls, Δy^+ varied from about 0.04 at the wall to 4.57 at the centre of the duct, while in the streamwise direction, the grids were

uniformly spaced with $\Delta x^+ < 9$. The superscript, $+$ refers to normalisation by wall units defined in terms of the local friction velocity at the centre of the moving wall. The time steps employed were such that CFL number was less than 0.3. In this study, we introduce a Reynolds number, Re_w, given by the expression: $Re_w = U_w h/\nu$, where U_w is the velocity of the moving wall.

III. CRITICAL CONDITIONS FOR SELF-SUSTAINED TURBULENCE

We seek to determine the critical Reynolds number (Re_c) for transition to turbulence and also obtain an estimate of the typical length scales (L_c) of the smallest structures required for the sustenance of a turbulent state in wall-driven square duct flow. The value of L_c places a lower bound on the length of the box that can be used for a turbulent flow simulation. Given the sub-critical nature of the transition, initial conditions are very important. Following the approach of Jimenez and Moin[15], Hamilton *et al.*[16] and Uhlmann *et al.*[10], the simulations were initiated using, as starting conditions, the fully developed turbulent flow field at a high Reynolds number and/or duct length (L_x). The Reynolds number was then gradually varied in successive runs while keeping L_x constant until the flow re-laminarised. In other cases, L_x was varied while holding Re_w constant. The fluctuations in the streamwise and wall-normal velocity at different locations in the duct were monitored; upon re-laminarisation, these dropped to zero. In each simulation, the flow was allowed to evolve for a time of at least 3500 h/U_w. Similar integration times have been employed by Refs. 10 and 15 in their studies on turbulence sustenance in minimal flow units.

Figure 2 shows the flow states for different combinations of Re_w and L_x. The data points at the boundary between laminar and turbulent states are connected with dashed lines. For turbulent states away from this boundary, a mesh with 96×96 cross-sectional divisions was found to be sufficient to obtain a sustained turbulent state. At $Re_w = 1500$ and $L_x = 4\pi h$, we compared the turbulence statistics obtained using this grid with that from a grid having 128×128 cross-sectional divisions and obtained good agreement. In both cases, the number of cells in the streamwise direction (N_x) was equal to 160. The data also agreed well with those in a duct of length $12\pi h$ (having $96 \times 96 \times 352$ cells). However, two-point correlations showed that a decorrelation of the streamwise velocity fluctuations was not achieved with $L_x = 4\pi h$.

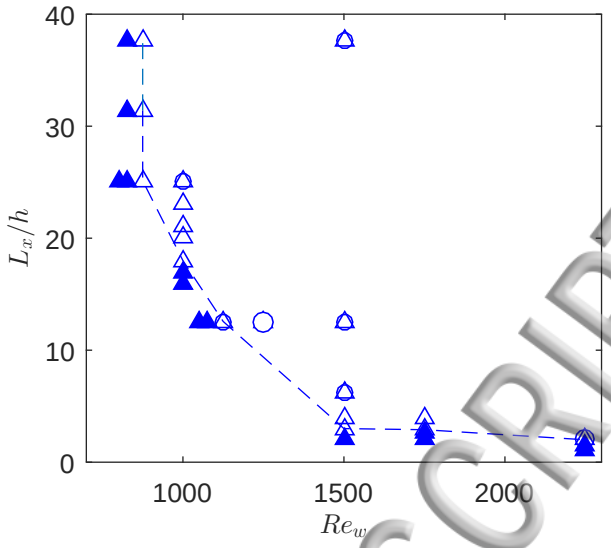

FIG. 2. Critical conditions for turbulence. Filled symbols represent laminar states while unfilled ones are the turbulent states. △, $N_z = N_y = 128$ grid cells; ◯, $N_z = N_y = 96$ grid cells; - - - -, laminar/turbulent boundary.

From Fig. 2, it can be observed that the lowest Reynolds number (Re_c) at which a turbulent state can be sustained is about 875. For values of Re_w less than this, a re-laminarisation of the flow occurred irrespective of the domain length. Given that the same result was obtain in boxes of length $8\pi h$, $10\pi h$ and $12\pi h$, we do not expect to see a large change in the estimated value of Re_c in a longer box. However, there is an uncertainty of about ± 25 (since the Reynolds number was varied in steps of 50). We further check that Re_c is independent of the grid by repeating the simulation at $Re_w = 825$ (the laminar data point just before Re_c) using two different meshes having 128×128 and 256×256 cells in the cross-sectional plane and 320 cells in the streamwise direction and a re-laminarisation of the flow was observed in both. We also check the grid independence of L_c at the Reynolds numbers considered, by repeating the cases where re-laminarisation occured, with a grid having 128×128 cross-sectional divisions. Table I gives the parameters for the eight data points connected by the dashed line in Fig. 2.

The transition Reynolds number is much greater than that in plane Couette flow ($Re_c \approx 370$, see Refs. 17 and 18), thus underscoring the importance of side walls in stabilising the flow. For large aspect ratio ducts, where end effects are negligible, Re_c is expected to be similar to that in plane Couette flow. To verify this, we carried out simulations in two

TABLE I. Simulation parameters for data points on the laminar/turbulent boundary. L_x is the length of computational domain Δy^+ is the grid resolution along the bisector of the moving wall and Δx^+, is that in the streamwise direction. N_x, N_y and N_z are the number of grid points in the x, y and z directions, respectively. Re_τ **is defined in terms of the average value of the shear stress at the centre plane of the moving walls.**

Re_w	L_x	$N_y \times N_z \times N_x$	Re_τ	Δy^+	Δx^+
875	$12\pi h$	$128 \times 128 \times 352$	52	$0.04 - 1.91$	5.80
875	$10\pi h$	$128 \times 128 \times 320$	52	$0.04 - 1.91$	5.16
875	$8\pi h$	$128 \times 128 \times 320$	53	$0.04 - 1.92$	4.17
1000	$18h$	$128 \times 128 \times 192$	59	$0.04 - 2.16$	5.60
1125	$4\pi h$	$96 \times 96 \times 160$	65	$0.07 - 2.50$	5.19
1125	$4\pi h$	$128 \times 128 \times 160$	65	$0.05 - 2.38$	5.19
1500	$3h$	$128 \times 128 \times 96$	88	$0.07 - 3.21$	2.81
1750	$3h$	$128 \times 128 \times 64$	101	$0.08 - 3.69$	4.89
2250	$2h$	$96 \times 96 \times 64$	125	$0.13 - 4.65$	4.52
2250	$2h$	$128 \times 128 \times 64$	125	$0.10 - 4.57$	4.04

ducts of aspect ratios 2:1 and 4:1 having a length of $4\pi h$ and observed a turbulent state to be maintained at Re_w as low as 625 and 500, respectively. For the pressure-driven case, Vinuesa *et al.*[19] suggested that a duct with an aspect ratio of at least 24 is required to obtain results comparable to those in a channel. We thus expect that a similar aspect ratio will be required in Couette flow.

Close to transition, L_c can be observed to be larger than at higher Reynolds numbers, thus indicating an increase in the length scales of the turbulence structures; hence longer computational boxes are needed for the simulations. For $Re_w > 1500$, L_c is about $3h$. The flow in such minimal units are not realisable in the laboratory; rather, they are the basic building blocks of wall-bounded turbulent flows.[15] To simulate a physically realisable turbulent flow, the domain length would have to be much longer than L_c such that a decorrelation of the turbulence statistics is achieved.

IV. TURBULENT FLOWS AT LOW REYNOLDS NUMBERS

Having determined the critical conditions for self-sustained turbulence, we investigate the flow at relatively low turbulent Reynolds numbers. In the following sections, we present results obtained at $Re_w = 1500$ in a computational domain of length $12\pi h$. We have checked that this box is long enough to allow for the decorrelation of velocity fluctuations. A mesh having $96 \times 96 \times 352$ cells have been used. For this grid we have verified that the cell sizes are of the order of the Kolmogorov length scale (η) given by $\eta = (\nu^3/\epsilon)^{1/4}$, where ϵ is the rate of turbulent kinetic energy dissipation. At the wall, ϵ was estimated from the viscous diffusion term in the turbulent kinetic energy equation[20] but away from the wall, ϵ was obtained by assuming turbulent kinetic energy production to be equal to dissipation. From this analysis, the grid resolution ranged from about 0.16η to 1.8η. Along the bisector of the moving walls, Δy^+ varied from about 0.09 at the wall to 4.05 at the centre of the duct, while in the streamwise direction, Δx^+ was about 8.91.

A. Secondary flow pattern

Figure 3 shows the mean velocity fields, the velocity vectors indicating the secondary flow pattern. An alternation of the flow field in time between two states can be observed, one being a mirror reflection of the other, and the flow remaining approximately symmetrical about the common bisector of the moving walls (see Figs. 3(a) and (b)). We hereafter refer to the state corresponding to Fig. 3(a) as A and that shown in Fig. 3(b) as B. In either case, a pair of large counter-rotating vortices associated with a moving wall dominates the entire flow field, transporting momentum from the wall to the interior of the duct, and another pair of smaller vortices is located at the opposite wall. The time spent in each state can be rather long. The velocity fields in Figs. 3(a) and (b) have been obtained by averaging over two separate intervals, of lengths $1050h/U_w$ and $1506h/U_w$, respectively during which the flow was continuously in each state. As the flow switches states, the large vortices shrink and are pushed towards the corners, while maintaining their rotation sense and the vortex pair at the opposite wall become enlarged. Averaging over long times result in a four-vortex secondary flow pattern, symmetrical about the wall bisectors (see Fig. 3(c), where the integration time is $12960h/U_w$).

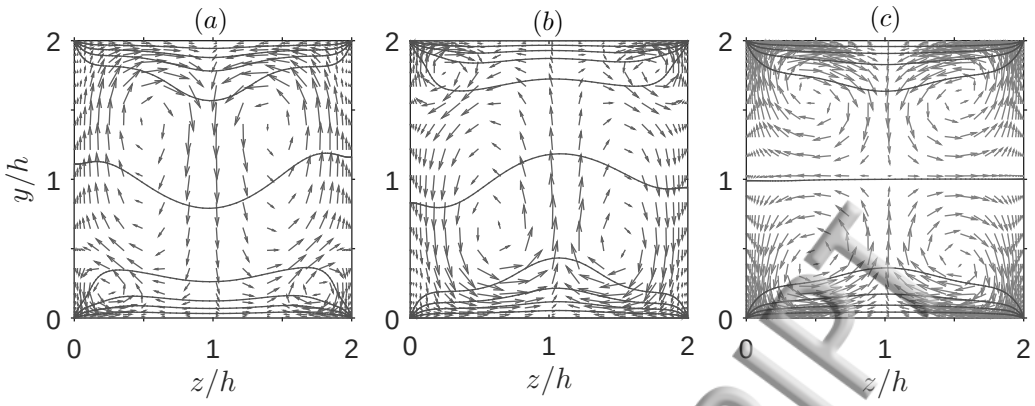

FIG. 3. Contours of mean streamwise velocity normalised by the wall velocity, U_w, and secondary flow vectors at $Re_w = 1500$ and $L_x/h = 12\pi$: (a) averaging interval $1050h/U_w$, (b) average over a different interval of length $1506h/U_w$ (flow is in a different state),(c) averaging interval $12960h/U_w$ (including both previous intervals). Contours range from -1 at the **lower wall to 1 at the upper wall**, with increment 0.2. For clarity, vectors are shown at every third grid point.

To quantitatively identify the two states, we define the magnitude $S(t)$ of the secondary flow in the central part of the duct, assigning a sign depending on the value of the wall-normal velocity component:

$$S(t) = \begin{cases} \sqrt{\tilde{v}^2 + \tilde{w}^2}, & \tilde{v} > 0 \\ -\sqrt{\tilde{v}^2 + \tilde{w}^2}, & \tilde{v} < 0, \end{cases} \tag{3}$$

where the tilde symbol represents instantaneous spatial averaging in the streamwise direction. We introduce an indicator function given by:

$$I(t) = \frac{\iint_R S(t) dydz}{\iint_R |S(t)| dydz}, \tag{4}$$

where R is the region bounded by the lines $z/h = 0.6$, $z/h = 1.4$ and the upper and lower walls, where the secondary flow is mostly in the direction normal to the moving walls (see Fig. 3(a) and (b)). $I(t)$ ranges between -1 and 1, negative values corresponding to state A and positive values, B. Based on the above criteria, conditional averaging was carried out to separate the two states. Figure 4 shows the evolution of the indicator function over the interval for which the flow fields in Fig. 3 have been computed. The average values of I in Figs. 3(a) and (b) are -0.775 and 0.709, respectively. The change in state can be observed

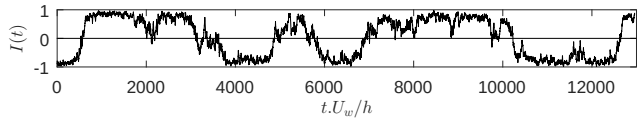

FIG. 4. variation of the indicator function, $I(t)$ with non-dimensional time at $Re_w = 1500$ and $L_x/h = 12\pi$

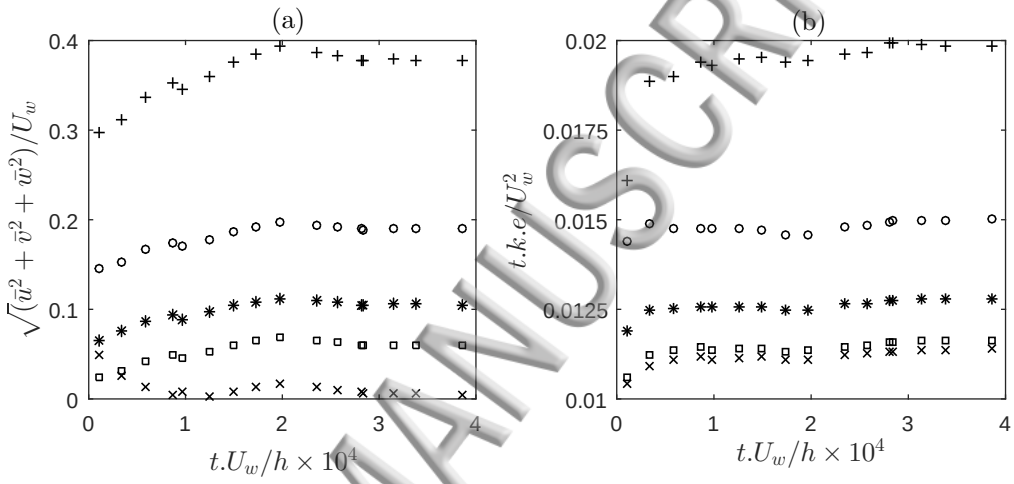

FIG. 5. Convergence test: (a) mean velocities computed from different integration times; (b) turbulent kinetic energy computed from different integration times. Data along the moving-wall bisector is presented. $\times$, $y/h = 1.0$; $\square$, $y/h = 1.2$; *, $y/h = 1.4$; $\circ$, $y/h = 1.6$; +, $y/h = 1.8$.

to occur in an irregular fashion; however, the time spent in each state is of the order of $1000h/U_w$.

Statistical convergence of the long-time-averaged flow fields was checked by computing the velocity magnitude and turbulent kinetic energy (t.k.e) from data accumulated over different times (see Fig. 5 where data along the moving-wall bisector is shown). The simulation was run for a period of up to $38650h/U_w$. For times greater than $28140h/U_w$, the differences in the computed statistics were found to be less than 1%, hence the analyses in the following sections are based on flow fields accumulated over integration periods larger than $28140h/U_w$.

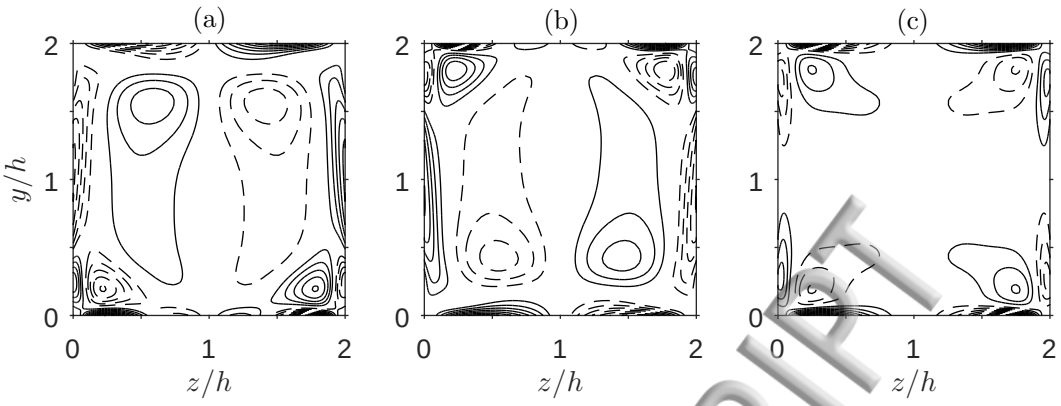

FIG. 6. Contours of mean streamwise vorticity at $Re_w = 1500$. (a) and (b) correspond to states A and B, respectively, while (c) is the contour plot for the long-time-averaged flow field. **The data have been normalised** by the maximum absolute vorticity; contours range from -1 to 1 with increment 0.1; negative values dashed. Length of computational domain is $12\pi h$.

B. Origin of the secondary flow

Associated with the secondary flows in non-circular ducts is a mean streamwise component of vorticity; hence by examining the vorticity transport equation, an insight into the origin of these motions can be obtained. For fully developed flow in a straight duct, the equation reads

$$\underbrace{\overline{v}\frac{\partial\bar{\Omega}_x}{\partial y}+\overline{w}\frac{\partial\bar{\Omega}_x}{\partial z}}_{C}-\underbrace{\nu\left(\frac{\partial^2}{\partial y^2}+\frac{\partial^2}{\partial z^2}\right)\bar{\Omega}_x}_{D}+\underbrace{\left(\frac{\partial^2}{\partial y^2}-\frac{\partial^2}{\partial z^2}\right)\overline{v'w'}}_{P_1}+\underbrace{\frac{\partial^2}{\partial y\partial z}(\overline{w'^2}-\overline{v'^2})}_{P_2}=0, \qquad (5)$$

where $\bar{\Omega}_x = \frac{\partial\overline{w}}{\partial y} - \frac{\partial\overline{v}}{\partial z}$ is the mean streamwise vorticity, and the prime symbol as well as the overbars represent fluctuating velocity components and time averaging, respectively. The first two terms, C, on the left hand side of Eq. (5) represent the convection of streamwise vorticity by the secondary motion itself. Together with the viscous diffusion term, D, these quantities are mainly involved in the redistribution of vorticity within the duct. P_1 and P_2 represent the contribution of the Reynolds cross-stream shear stress and the anisotropy of the cross-stream normal stresses, respectively. They act to either produce or destroy streamwise vorticity.

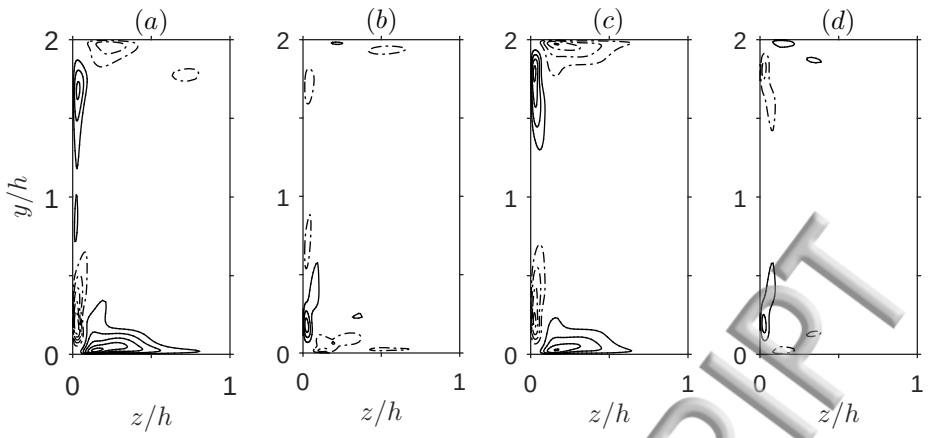

FIG. 7. Contours of production terms in the mean streamwise vorticity transport equation, normalised by $(U_w/h)^2$. (a) and (b) show the normal (P_2) and shear-stress (P_1) terms, respectively, while the flow is in state A. (c) and (d) show P_2 and P_1, respectively, for the long-time-averaged flow field. Contours range from -0.1 to 0.1, with increment 0.02; negative values dashed.

Figure 6 shows the contours of $\bar{\Omega}_x$. It can be observed that they closely match the secondary flow patterns shown in Fig. 3, except close to the walls where there is an inversion of the vorticity sign. The corner vortices are associated with higher values of vorticity, but the maximum is located on the moving wall. Figures 7(a) and (b) show the distribution of the normal and shear-stress terms of the vorticity transport equation, respectively, while the flow is in state A (note that the corresponding plots for state B can be obtained by a π rotation about the duct's axis). The plots for the long-time-averaged data are shown in Fig. 7(c) and (d). Since the flow is symmetrical about the common bisector of the moving walls, only half of the computational domain is shown. In state A, close to the lower corner, where the small vortices are located and across most of the lower wall, the contribution of P_2 to the production of streamwise vorticity can be observed to be larger than that of P_1. Its maximum value, which is about 1.8 times larger than the maximum P_1 occurs at $z/h = 0.023, y/h = 0.190$. However, at the upper wall, where the large vortices are located, P_1, though relatively small in magnitude, accounts for the vorticity production away from the corner. Switching between states results, in the long run, in a flow field in which streamwise vorticity production is dominated by gradients of the anisotropy of the Reynolds normal stresses (see Fig. 7(c) and (d)).

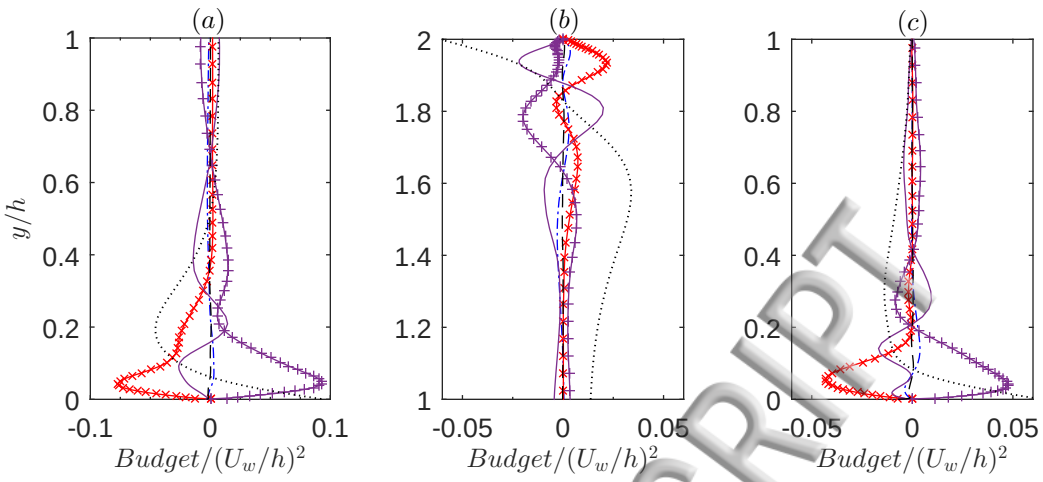

FIG. 8. Budget of terms in the mean streamwise vorticity transport equation along lines parallel to the side wall and passing through the centre of the vortices: (a) at $z/h = 0.25$, while the flow is in state A, (b) at $z/h = 0.6$ (same state as (a)), (c) at $z/h = 0.4$ in the long-time-averaged flow field. +, normal stress (P_2); ——, shear stress (P_1); ×, viscous diffusion; -.-.-, convection; - - - -, balance; ....., $\bar{\Omega}_x/(6U_w/h)$

The contributions of terms in Eq. (5) are quantitatively shown in Fig. 8. Plots of the streamwise vorticity are also included for reference. Consider a line parallel to the y axis, located at $z/h = 0.25$, and passing through the centre of the corner vortex. Close to the lower wall, the production of vorticity is dominated by the anisotropy term, P_2 (see Fig. 8(a)), the maximum value occurring at $y/h \approx 0.05$ where there is a change in the vorticity sign. P_2 is balanced by viscous diffusion and the shear-stress term which is much smaller in magnitude. It can be observed that the contributions of P_2 and P_1 are of opposite signs across most of the duct, one acting as a source term and the other, having the same sign as the viscous diffusion term, acting as a sink. Beyond $y/h \approx 0.36$, P_1 and P_2 are roughly of the same magnitude. The convection term is very small across the entire length shown, and so is D beyond $y/h \approx 0.36$. Figure 8(b) shows the terms in the vorticity transport equation along a vertical line, located at $z/h = 0.6$, passing through the centre of the large vortex associated with the upper wall. Close to the wall, P_1 can be observed to account for most of the vorticity production as earlier discussed, its maximum value occurring at $y/h \approx 1.94$. Again, balance is maintained by the viscous diffusion term, while the convection term is very small. Below $y/h \approx 1.94$, P_2 increases, attaining a maximum at $y/h \approx 1.79$, beyond which

is roughly of the same magnitude as P1. For the long-time-averaged flow field along a line passing through the centre of a secondary flow vortex at $z/h = 0.4$ (see Fig. 8(c)), a trend similar to that of Fig. 8(a) can be observed. From the foregoing, it can be concluded that gradients of the Reynolds secondary shear stress, $\overline{v'w'}$ away from the corners play a key role in the formation of the large secondary flow vortices. On the other hand, the corner vortices emerge as a result of gradients of $\overline{w'^2} - \overline{v'^2}$.

C. Flow statistics and turbulence structure

Streamwise velocity profiles along the moving-wall bisector, normalised by local friction velocity are presented in Fig. 9(a). The plane Couette flow data of Avsarkisov *et al.*[21] and Pirozzoli *et al.*[22] at $Re_\tau = 125$ and 171, respectively and duct flow experiment of Owolabi *et al.*[12] are also shown for the purpose of making comparison. In state A, at the lower half of the duct, the velocity profile can be observed to be in good agreement with those in the channel. The data matches the logarithmic scaling law: $|\bar{u} - U_w|^+ = 2.44\, ln(y^+) + 5.1$, in the region: $30 < y^+ < 69$. At the duct's upper half (equivalent to the lower half in state B), however, an overshoot from the log law can be observed. As will be shown later, the local shear stress at the upper moving wall is smaller than at the lower one. Therefore, normalising by the local friction velocity results in higher non-dimensional velocities being obtained. Furthermore, the Reynolds number based on the local friction velocity ($Re_\tau = 70$) is smaller than at the lower wall ($Re_\tau = 90$) hence this deviation from the classical profile is a low Reynolds number effect. For the long-time-averaged flow field, the velocity profile lies between those of the bi-stable states.

Root mean square velocity fluctuations along the moving-wall bisector normalised by the wall velocity are shown in Fig 9(b). Larger streamwise fluctuations can be observed across most of the duct in the long-time-averaged flow field. These are induced by the intermittency in the flow. In one state, the velocities fluctuate about a mean which is higher than the long-term one, while in the other, the fluctuations are about a mean value lower than the long-time-average. Hence in the long run, the deviations from the long-term mean are large (see Fig. 10, where the probability density functions of instantaneous streamwise velocity at $y/h = 0.4$ are shown). In state A, the peaks in u_{rms} ($u_{rms}/U_w \approx 0.172$ and 0.170 near the lower and upper walls, respectively) can be observed to be slightly higher than that

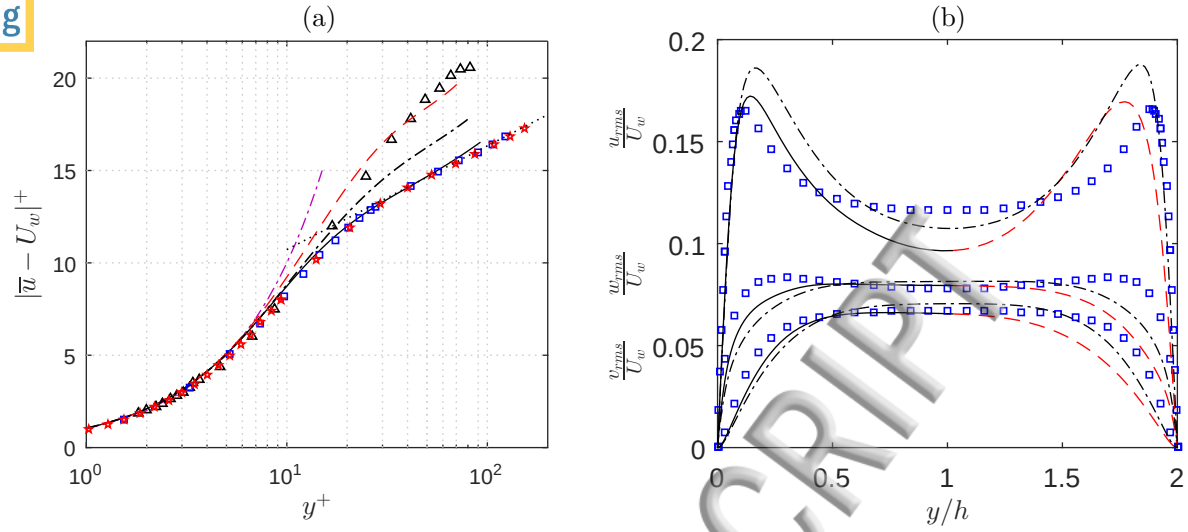

FIG. 9. Turbulence statistics: (a) Streamwise velocity profiles, (b) Root-mean-square velocity fluctuations. ——, profile from **lower half** of duct while the flow is in state A; - - - -, profile from **upper half** of the duct while the flow is in state A; -.-.-.-, long-time-averaged flow field; □ , Plane Couette flow DNS of Ref. 21 at $Re_\tau = 125$; ⋆, plane Couette flow DNS of Ref. 22 at $Re_\tau = 171$; △ square duct flow exp. of Ref. 12; -.-.-.-, $|\bar{u} - U_w|^+ = y^+$; ....., $|\bar{u} - U_w|^+ = 2.44.ln(y^+) + 5.1$.

in the plane Couette flow data of Avsarkisov *et al.*[21] ($u_{rms}/U_w \approx 0.165$). At the lower wall, the maximum u_{rms}/U_w exists closer to the wall than at the upper wall. As earlier shown, the Reynolds numbers based on the local friction velocity is larger at the bottom, hence this trend is consistent with findings in wall-bounded turbulent flows which show an inward shift of the peak with increasing Reynolds number. A similar argument applies to the wall-normal velocity fluctuations which can be observed to be higher close to the lower wall. Here, v_{rms}/U_w and w_{rms}/U_w are slightly greater than those of the long term averaged flow field. The converse is the case close to the upper wall. As the duct's centre is approached, u_{rms}/U_w drop to lower values than in the channel while v_{rms}/U_w and w_{rms}/U_w are very similar to those in the channel.

Next, we consider the invariants of the non-dimensional Reynolds stress anisotropy tensor given by:

$$II = b_{ij}b_{ji}/2, \qquad III = b_{ij}b_{jk}b_{ki}/3, \tag{6}$$

where

$$b_{ij} = \overline{u_i'u_j'}/\overline{u_k'u_k'} - \frac{1}{3}\delta_{ij}. \tag{7}$$

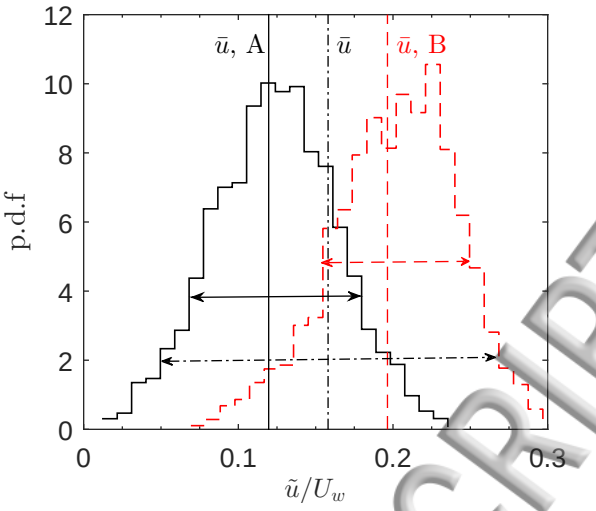

FIG. 10. Probability density function of instantaneous streamwise velocity, $\tilde{u}$, at $y/h = 0.4$. Legend as in Fig. 9. Arrows indicate fluctuations about the short and long-time averages.

All possible turbulence states must lie within the Lumley triangle,[23] bounded by the lines: $-II/3 = (III/2)^{2/3}$, $-II/3 = (-III/2)^{2/3}$ and $-II = 3(1/27 + III)$, corresponding to axisymmetric expansion, axisymmetric contraction and two-component turbulent states, respectively,[24] while the bottom, left and right vertices represent the three-component isotropic, two-component axisymmetric and one-component limits, respectively. It should be noted that these do not relate to the shape of the turbulent eddies; rather, they give an indication of the state of the Reynolds stress tensor. Figure 11 shows the anisotropy invariant map (AIM) for the long-time-averaged flow field as well as the plane Couette flow data of Avsarkisov *et al.*[21] at $Re_\tau = 125$. Data for only half of the duct is shown. Along the moving-wall bisector (see Fig. 11(a)), the AIM is not very different from that in plane Couette flow (Fig. 11(b)). Close to the wall, due to the damping of wall-normal velocity fluctuations, the turbulence is two-dimensional but at $y^+ \approx 7.6$ ($y^+ \approx 7.3$ in the plane Couette data), there is a switch to an axisymmetric state. As the centre of the duct is approached, the turbulence becomes increasingly isotropic due to the closeness of the fluctuations in all velocity components (see Fig. 9(b)). The level of isotropy at the centre is however higher in the square duct.

The variation of shear stress along the moving walls while the flow is in state A, as well as that in the long-time-averaged flow field are shown in Fig. 12(a). The plots have been normalised by the long-term mean at the centre of the moving wall, τ^*. Close to the

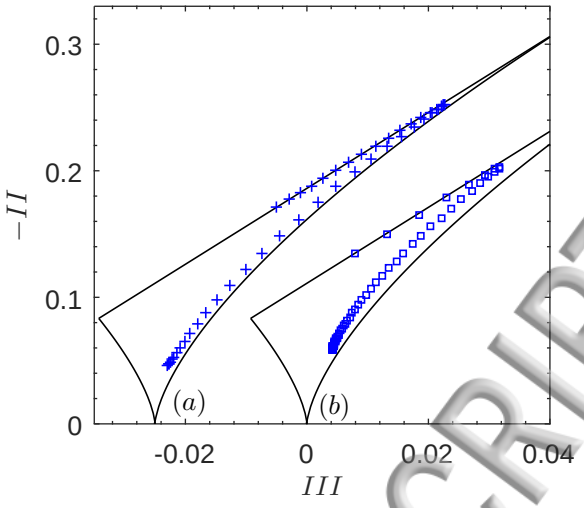

FIG. 11. Anisotropy invariant maps. (a) At $z/h = 1$ (b) Plane Couette flow data of Ref. 21.

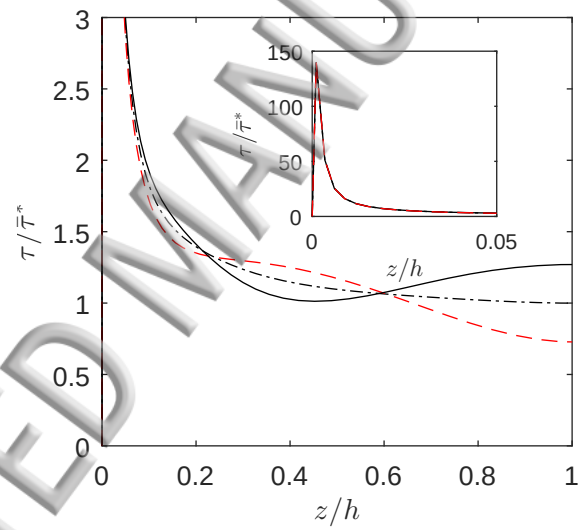

FIG. 12. Wall shear stress distribution at the moving walls. Flow is in state A: ———, **lower wall**; - - - -, **upper wall**; -.-.-.-.-, long-time-averaged flow field. Only half of the duct is shown, due to symmetry about the moving-wall bisector.

corners, the stresses increase dramatically (see inset of Fig. 12(a)). Slow-moving fluid at the stationary side walls interact with fast-moving fluid at the moving wall, resulting in large velocity gradients. At the lower wall, the shear stress drops to a local minimum at $z/h = 0.45$ before approaching a local maximum at $z/h = 1$, while at the upper wall, a local minimum is found at the duct centre. As the flow switches to state B, the profiles

become interchanged, hence no distinct extrema can be observed in the long-time-averaged flow field.

Figures 13(a) and (b) show the typical instantaneous velocity fields at x-z planes close to the lower and upper walls in the bi-stable states (In this case, the data for state A is presented). As earlier shown, Re_τ for this flow is as low as 70. This corresponds to a duct width of about 140 in wall units. Given that the separation distance of coherent structures in a turbulent flow is about 100 wall units[27], the duct is just barely wide enough to host the structures required to maintain a turbulent state. The figures reveal the existence of only a single high-speed streak centrally positioned along the upper wall and two at the lower wall, close to the corners. Hence the switching between states occurs in such a way as to increase the number of structures close to a given wall, to ensure continued sustenance of turbulence. The position of the streaks correspond to the wall shear stress extrema locations. To clearly show them, we present data at y/h=0.2 and y/h=1.8, corresponding to locations of large u_{rms}. The structures are persistent over the length of the duct, indicating that the states are very stable in the streamwise direction. Associated with each streak is a pair of counter-rotating vortices. Figure 13 (c) shows a snapshot of the instantaneous velocity field in the cross-sectional plane of the duct at $x/h = 20$ where the two streaks in Fig.13 (b) are clearly separated. The high-speed streaks, indicated by mushroom-shaped velocity contours, can be observed to be positioned between the vortices. They are formed due to the lift-up of high speed flow by the vortices from the wall. These coherent structures have been shown to play a crucial role in the turbulence regeneration cycle.[25]. When averaged in space and time, they result in the observed secondary flow pattern in a square duct.

Figure 14 shows the results of quadrant analysis carried out to determine the contribution of various turbulent events to the Reynolds shear stress, $\overline{u'v'}$. The Reynolds shear stress can be divided into four quadrants (Q1-Q4) depending on the sign of velocity fluctuations (see inset of figure 14(a)). In the analysis, the coordinate system was modified such that positive v always pointed away from the nearest moving wall, while u was always positive in the translation direction of the nearest moving wall. In state A, along the bisector of the upper wall, Q1 events representing the ejection of fast-moving fluid away from the wall by positive wall-normal velocity fluctuations dominate. This is also the case at the lower wall, close to the corners (see Fig. 14(b) where data along the line $z/h = 0.45$ passing through a region where the secondary flow vectors are pointed away from the wall is

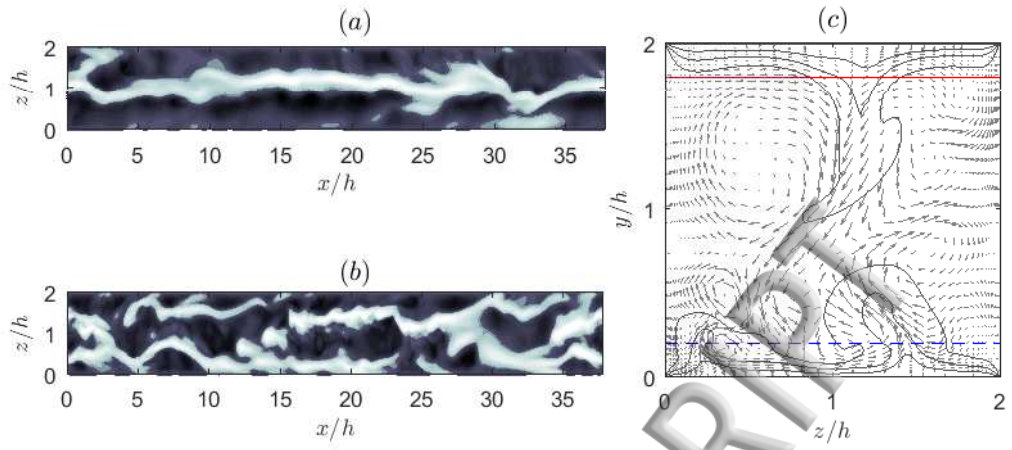

FIG. 13. Coherent structures. (a) and (b) are typical instantaneous velocity fields (not to scale) at $x-z$ planes located at $y/h = 1.8$ and 0.2, respectively, corresponding to regions of large fluctuations in streamwise velocity ; white contours indicate $u' > 0$ and black, $u' < 0$. Only fluctuations larger than 40% of the maximum in each plane are shown. (c) is the velocity field in the duct's cross-section at $x/h = 20$. - - - -, $y/h = 0.2$; ——, $y/h = 1.8$

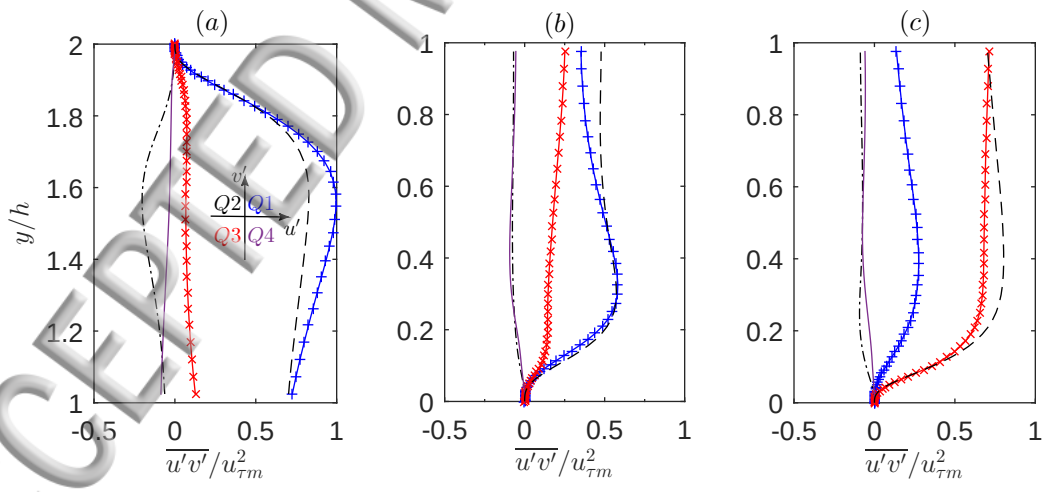

FIG. 14. Quadrant analysis of the Reynolds shear stress, while the flow is in state A: (a) along the **bisector of the upper wall**, (b) at $z/h = 0.45$ (line passes through a region where the secondary flow vectors are pointed away from the **lower wall**), (c) along the bisector of the lower wall. +, Q1; -.-.-, Q2; ×, Q3; ——, Q4; - - - - -, $\overline{u'v'}$ total.

presented). However, along the bisector of the lower wall, Q3 events representing sweeping motion during which slow moving fluid is conveyed to the wall by negative wall-normal fluctuations account for the bulk of $\overline{u'v'}$ generation (see Fig. 14(c)). A closer examination of the velocity fields in Fig.3(a) reveals that along the bisector of the upper wall (where quadrant analysis shows ejection events to dominate), the secondary flow can be observed to transport momentum away from the wall, causing the axial velocity contour to bulge towards the duct's interior. Similarly, at the lower wall (where sweeeping motion dominates), the secondary flow transports momentum towards the wall, causing the contours of axial velocity to bulge inwards. It is thus evident that the secondary motion is closely related to the near-wall ejection and sweeping events.

V. CONCLUSION

In this study, direct numerical simulations of turbulent Couette flows in a square duct at relatively low Reynolds numbers have been carried out. The flow is driven by a pair of opposite counter-moving walls translating with the same speed, resulting in a zero net transport of fluid through the duct. A turbulent state was found to be maintained only for Reynolds numbers greater than about 875. This is much higher than the $Re_c \approx 360 - 375$ observed in plane Couette flow studies,[17,18,26] thus underscoring the stabilising effect of the side walls on the flow. At Reynolds numbers close to the critical, the flow was observed to exist in two states, one being a mirror reflection of the other, with symmetry about the common bisector of the moving walls. In these states, the secondary motion (which is different from that in Poiseuille flow) is characterised by four vortices, induced by gradients of the anisotropic Reynolds normal stresses, $\overline{w'^2} - \overline{v'^2}$ and cross stream shear stress, $\overline{v'w'}$. Due to the intermittency in the flow, large fluctuations in the velocity, about the long-term mean were observed. Instantaneous flow field visualisations reveal the existence of coherent structures which are persistent over the length of the duct, thus indicating that the states are very stable in the streamwise direction. Quadrant analysis at different locations in the duct indicate that the secondary flow is closely related to the near-wall ejection and sweeping events; ejection dominating in regions where the secondary flow transports momentum away from the wall and sweeping dominating in regions where momentum is transported towards the wall.

ACKNOWLEDGMENTS

The authors gratefully acknowledge the support of Taiwan Ministry of Science and Technology, National Tsing Hua University and National Centre of High Performance Computing of Taiwan.

REFERENCES

[1]J. Nikuradse, "Untersuchungen $\ddot{u}$ber die geschwindigkeitsverteilung in turbulenten str$\ddot{o}$mungen," VDI Forsch, 281 (1926).

[2]E. Brundrett and W. D. Baines, "The production and diffusion of vorticity in duct fow," J. Fluid Mech. 19, 375–394 (1964).

[3]B. E. Launder and W. M. Ying, "Secondary flows in ducts of square cross-section," J. Fluid Mech. 54, 289–295 (1972).

[4]A. Melling and J. H. Whitelaw, "Turbulent flow in a rectangular duct," J. Fluid Mech. 78, 289–315 (1976).

[5]H. Iacovides and B. E. Launder, "Computational fluid dynamics applied to internal gas turbine blade cooling: a review," Int. J. Heat Fluid Flow 16, 45—470 (1995).

[6]S. Gavrilakis, "Numerical simulation of low-Reynolds-number turbulent flow through a straight square duct," J. Fluid Mech. 244, 101–129 (1992).

[7]A. Huser and S. Biringen, "Direct numerical simulation of turbulent flow in a square duct," J. Fluid Mech. 257, 65–95 (1993).

[8]H. Zhang, F. X. Trias, A. Gorobets, Y. Tan, and A. Oliva, "Direct numerical simulation of a fully developed turbulent square duct flow up to Re_τ= 1200," Int. J. Heat Fluid Flow 54, 258–267 (2015).

[9]Y. H. Lee, L. M. Huang, Y. S. Zou, S. C. Huang, and C. A. Lin, "Simulations of turbulent duct flow with lattice Boltzmann method on GPU cluster," Comput. & Fluids. 168, 14-20 (2018).

[10]M. Uhlmann, A. Pinelli, G. Kawahara, and A. Sekimoto, "Marginally turbulent flow in a square duct," J. Fluid Mech. 588, 153–162 (2007).

[11]A. Pinelli, M. Uhlmann, A. Sekimoto, and G. Kawahara, "Reynolds number dependence of mean flow structure in square duct turbulence," J. Fluid Mech. 644, 107122 (2010).

[12]B. E. Owolabi, R. J. Poole, and D. J. C. Dennis, "Experiments on low-Reynolds-number turbulent flow through a square duct," J. Fluid Mech. 798, 398–410 (2016).

[13]H. W. Hsu, J. B. Hsu, W. Lo, and C. A. Lin, "Large eddy simulations of turbulent couette-poiseuille and couette flows inside a square duct," J. Fluid Mech. 702, 89101 (2012).

[14]W. Lo and C. A. Lin, "Mean and turbulence structures of couette-poiseuille flows at different mean shear rates in a square duct," Phys. Fluids 18, 068103 (2006).

[15]J. Jimenez and P. Moin, "The minimal flow unit in near-wall turbulence," J. Fluid Mech. 225, 213240 (1991).

[16]J. M. Hamilton, J. Kim, and F. Waleffe, "Regeneration mechanisms of near-wall turbulence structures," J. Fluid Mech. 287, 317348 (1995).

[17]F. Daviaud, J. Hegseth, and P. Bergé, "Subcritical transition to turbulence in plane couette flow," Phys. Rev. Lett. 69, 2511–2514 (1992).

[18]N. Tillmark and P. H. Alfredsson, "Experiments on transition in plane couette flow," J. Fluid Mech. 235, 89102 (1992).

[19]R. Vinuesa, P. Schlatter, and H. M. Nagib, "On minimum aspect ratio for duct flow facilities and the role of side walls in generating secondary flows," Journal of Turbulence 16, 588–606 (2015).

[20]H. Abe, H. Kawamura, and Y. Matsuo, "Direct numerical simulation of a fully developed turbulent channel flow with respect to the Reynolds number dependence," J. of fluids Eng. 123, 382–393 (2001).

[21]V. Avsarkisov, S. Hoyas, M. Oberlack, and J. P. Garca-Galache, "Turbulent plane couette flow at moderately high reynolds number," J. Fluid Mech. 751 (2014).

[22]S. Pirozzoli, M. Bernardini, and P. Orlandi, "Turbulence statistics in couette flow at high reynolds number," J. Fluid Mech. 758, 327–343 (2014).

[23]J. L. Lumley, "Computational modeling of turbulent flows," Adv. Appl. Mech. 18, 123–176 (1979).

[24]A. J. Simonsen and P. Å. Krogstad, "Turbulent stress invariant analysis: Clarification of existing terminology," Phys. Fluids 17, 088103 (2005).

[25]J. Jiménez and A. Pinelli, "The autonomous cycle of near-wall turbulence," Journal of Fluid Mechanics 389, 335–359 (1999).

[26]A. Lundbladh and A. V. Johansson, "Direct simulation of turbulent spots in plane couette flow," J. Fluid Mech. 229, 499516 (1991).

[27] J. Kim and P Moin and R. Moser, "Turbulence statistics in fully developed channel flow at low Reynolds number," J. Fluid Mech. 177, 133–166 (1987)

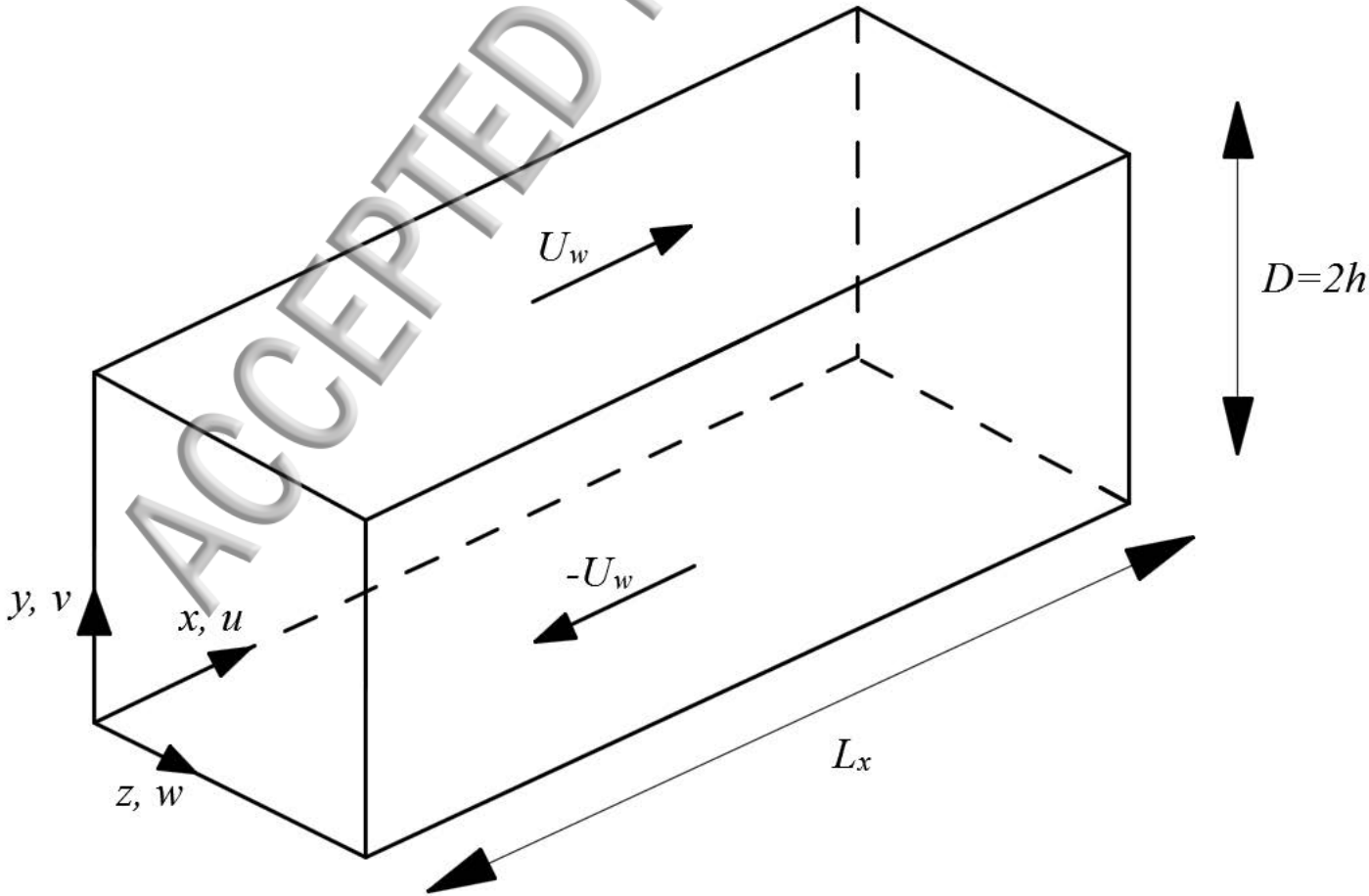

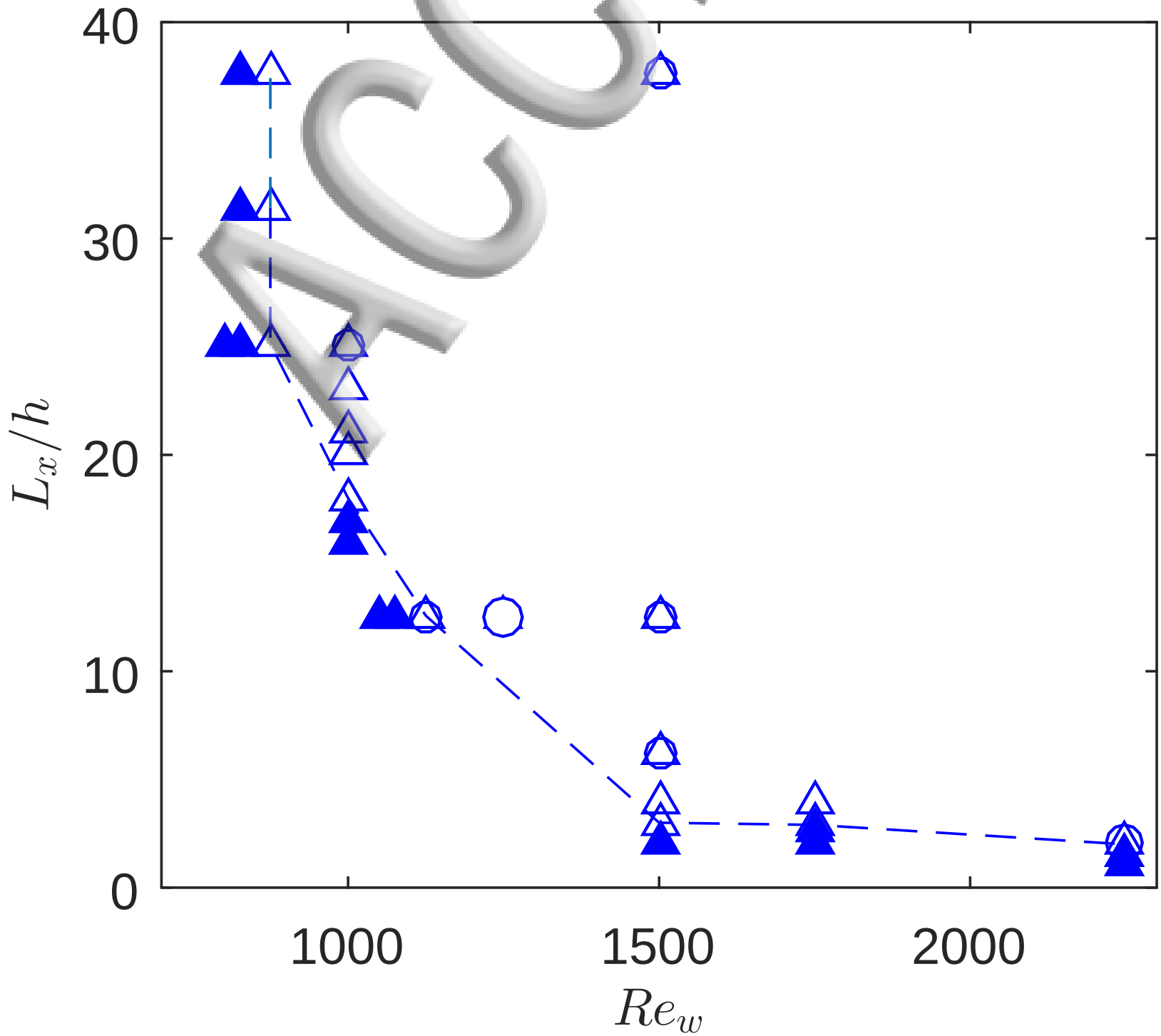
40
30
20
10
0
L_x/h
1000
1500
2000
Re_w

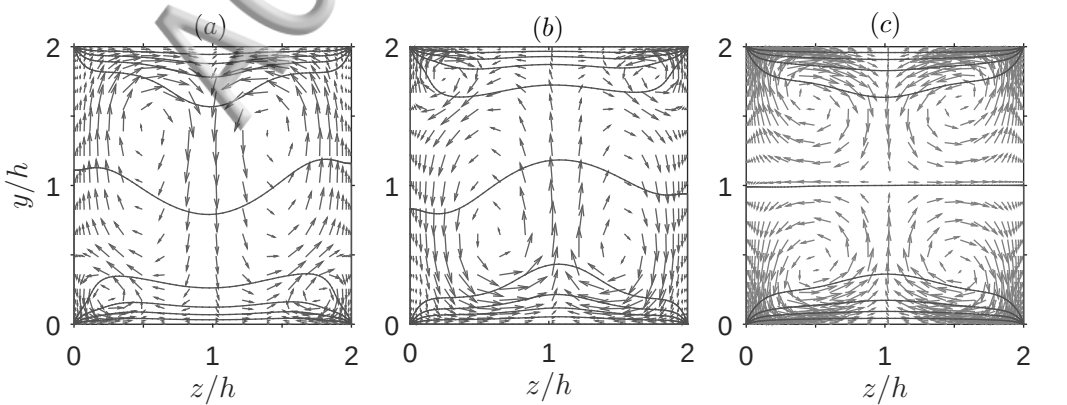
(a)
(b)
(c)
y/h
z/h
z/h
z/h
0
1
2

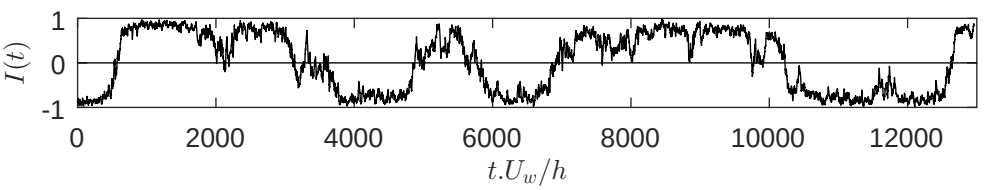

1
0
-1
$I(t)$
0
2000
4000
6000
8000
10000
12000
$t.U_w/h$

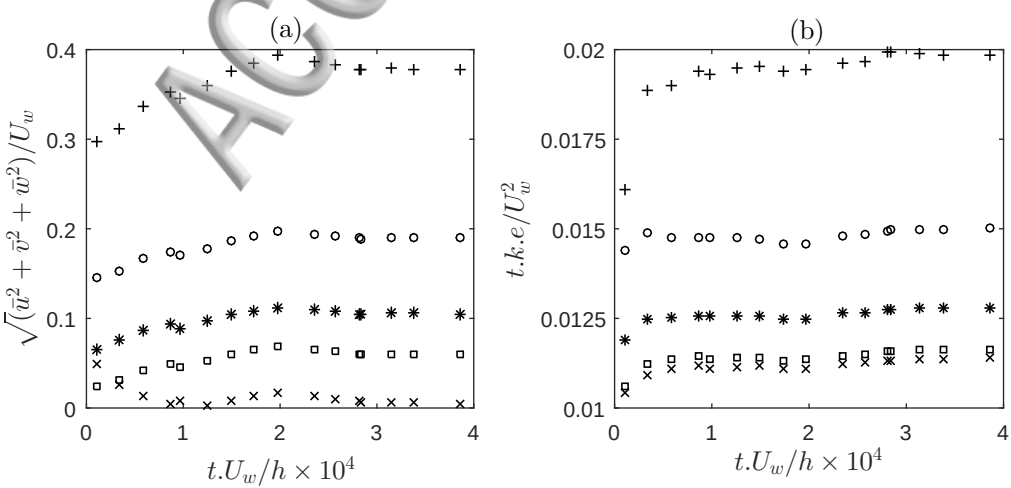
(a)
(b)
$\sqrt{(\bar{u}^2+\bar{v}^2+\bar{w}^2)}/U_w$
$t.k.e/U_w^2$
$t.U_w/h \times 10^4$
$t.U_w/h \times 10^4$
0.4
0.3
0.2
0.1
0
0.02
0.0175
0.015
0.0125
0.01
0
1
2
3
4

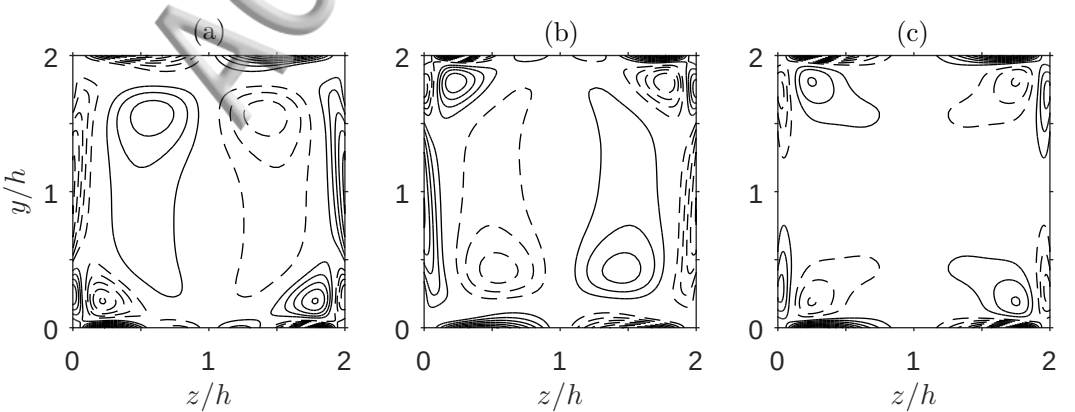
(a)
(b)
(c)
2
1
0
y/h
0
1
2
z/h

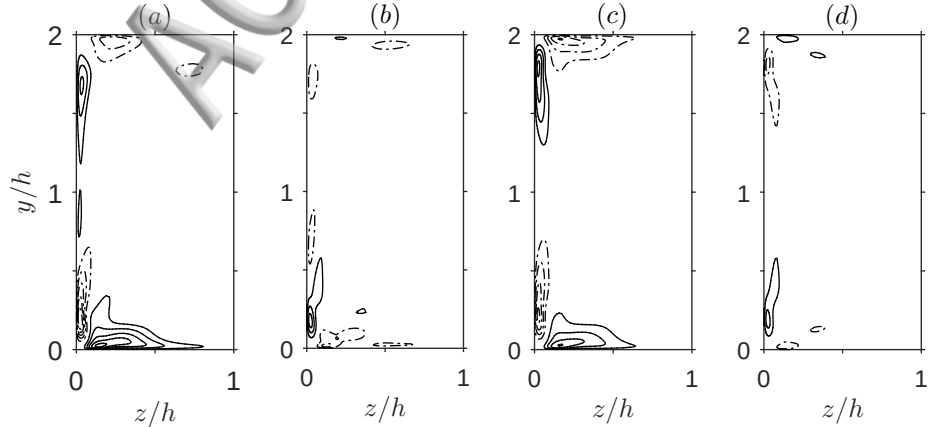
(a)
(b)
(c)
(d)
y/h
z/h
0
1
2

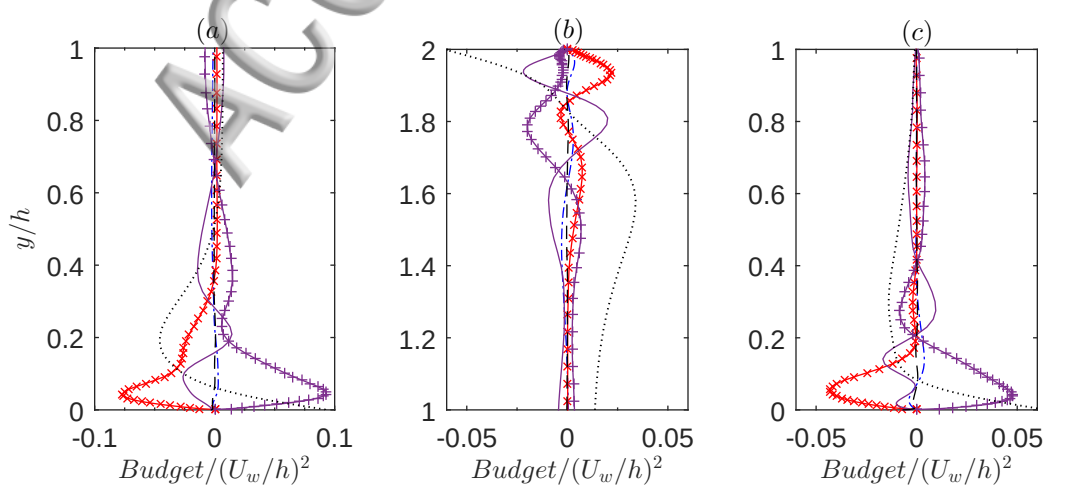
(a)
(b)
(c)
y/h
Budget/(U_w/h)^2
Budget/(U_w/h)^2
Budget/(U_w/h)^2

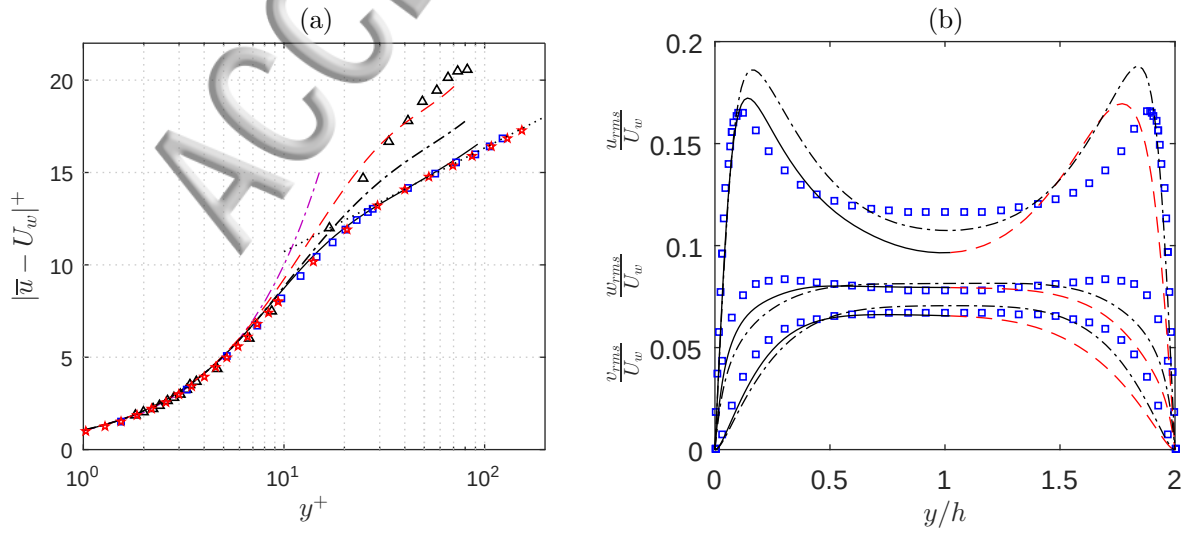
(a)
$|\overline{u} - U_w|^+$
y^+
10^0
10^1
10^2
0
5
10
15
20
(b)
$\frac{u_{rms}}{U_w}$
$\frac{w_{rms}}{U_w}$
$\frac{v_{rms}}{U_w}$
y/h
0
0.05
0.1
0.15
0.2
0.5
1
1.5
2

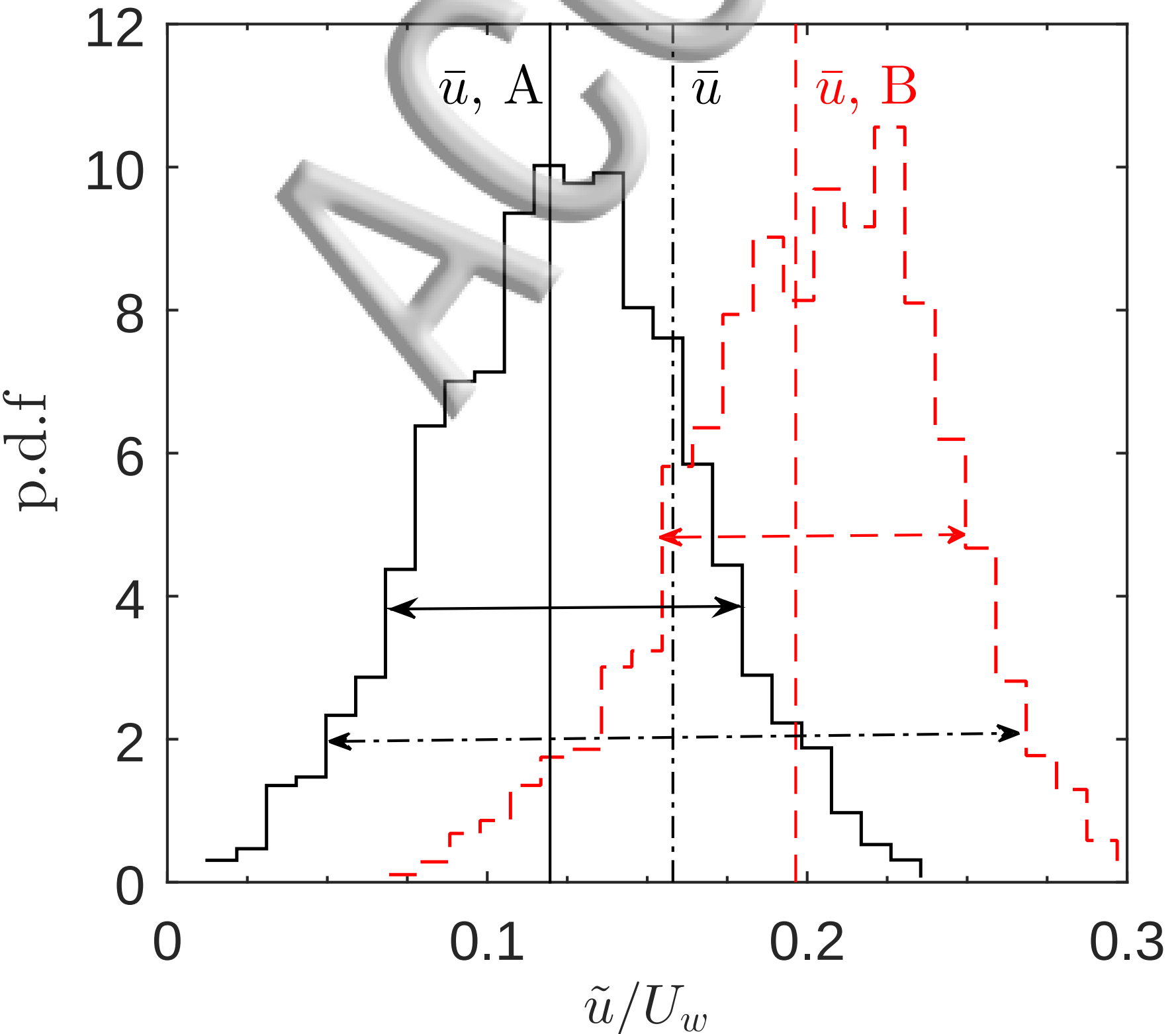
$\bar{u}$, A
$\bar{u}$
$\bar{u}$, B
p.d.f
$\tilde{u}/U_w$
0
2
4
6
8
10
12
0
0.1
0.2
0.3

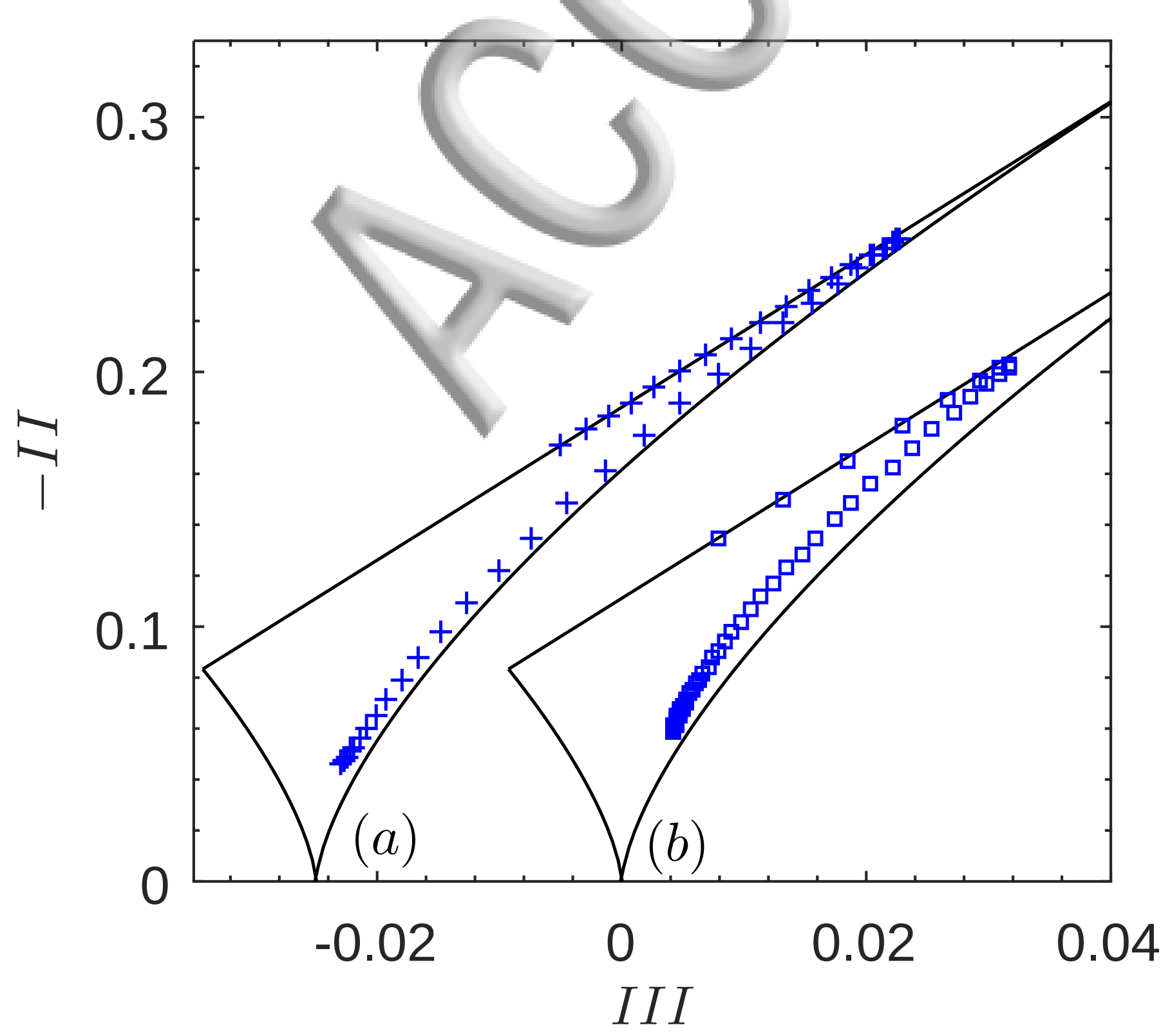
0.3
0.2
0.1
0
$-II$
-0.02
0
0.02
0.04
III
(a)
(b)

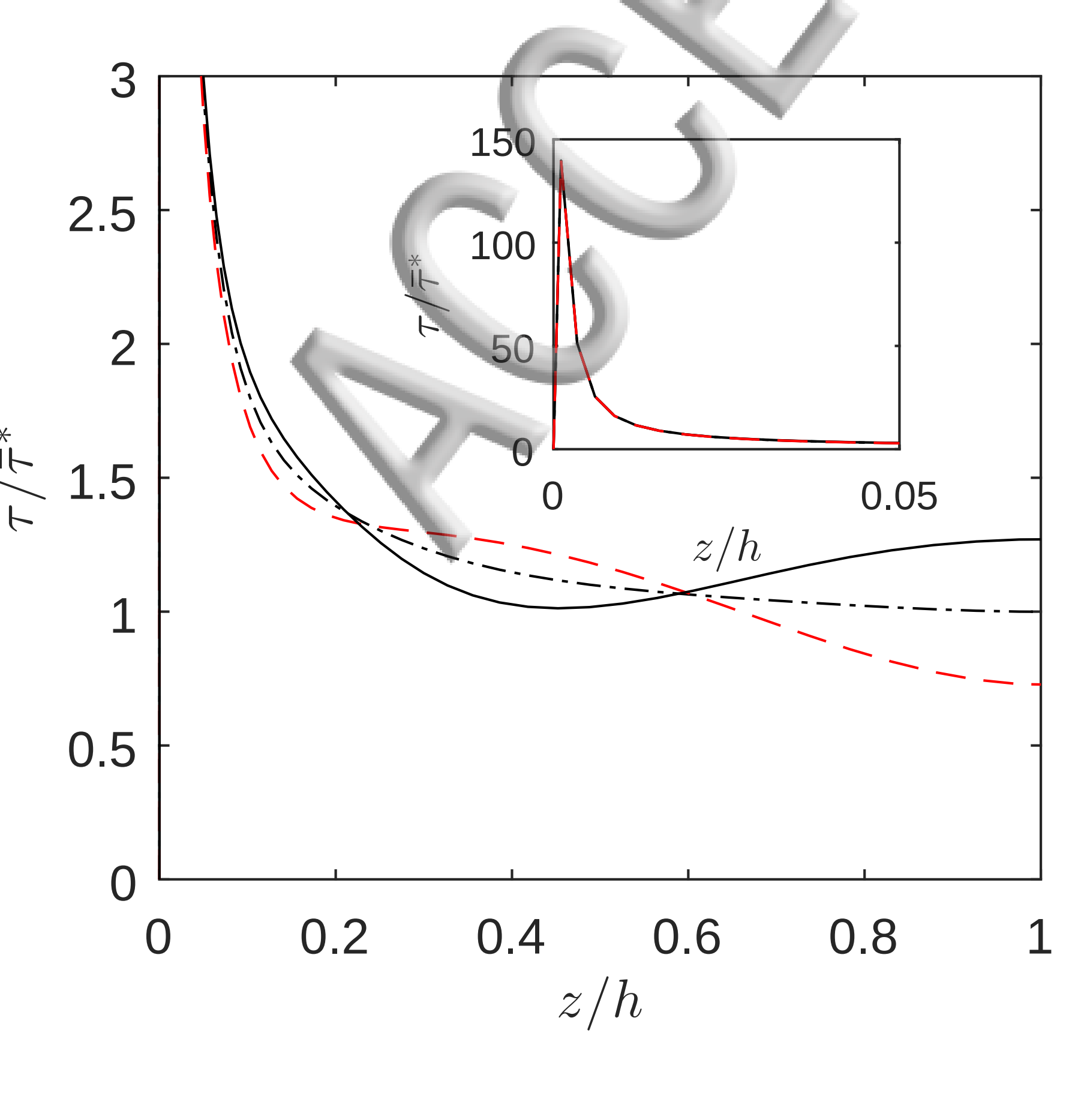
3
2.5
2
1.5
1
0.5
0
0
0.2
0.4
0.6
0.8
1
z/h
$\tau/\bar{\tau}^*$
150
100
50
0
0
0.05
z/h
$\tau/\bar{\tau}^*$

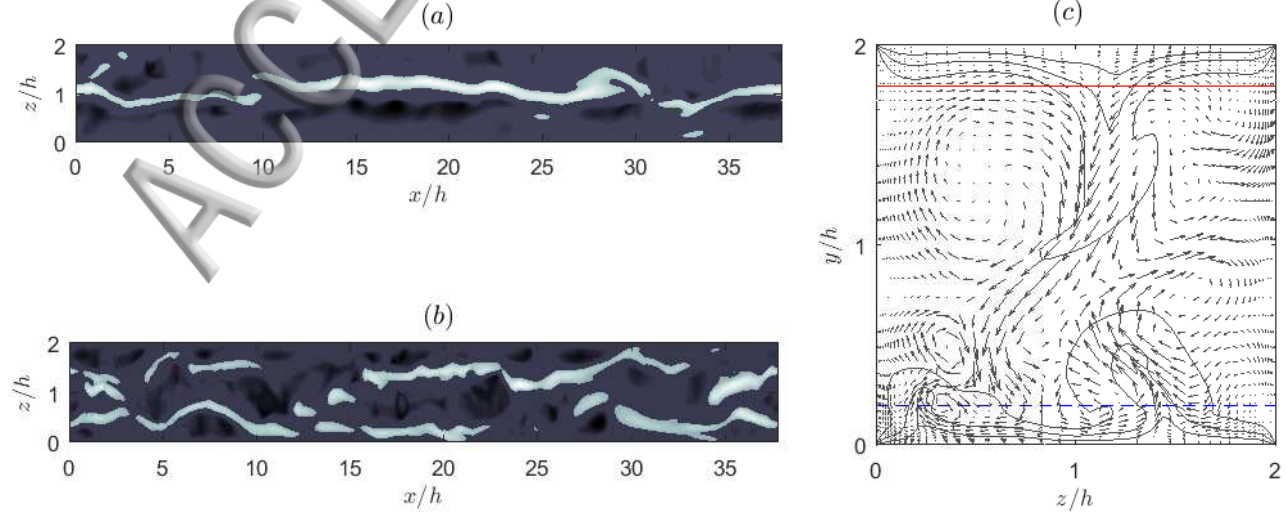

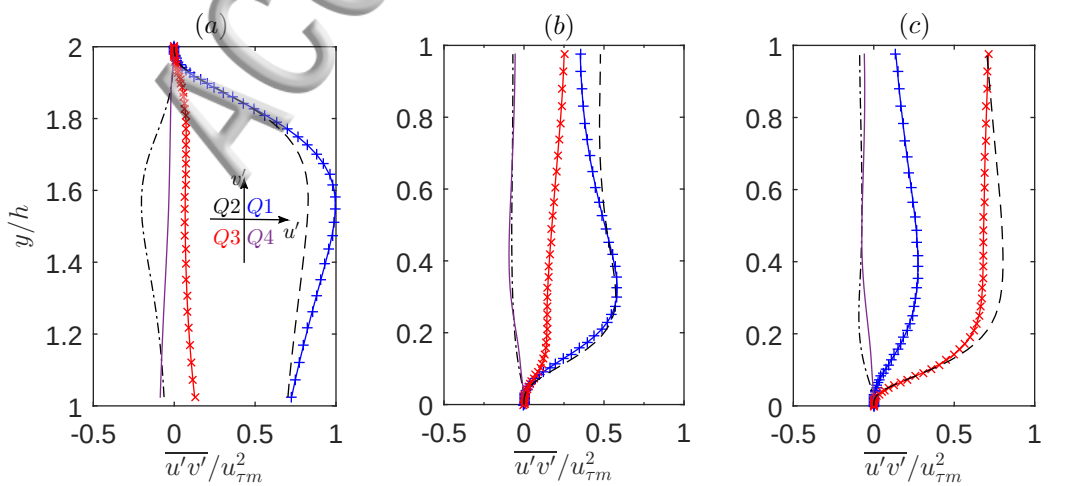
(a)
(b)
(c)
y/h
Q2
Q1
Q3
Q4
v'
u'
-0.5
0
0.5
1
0.2
0.4
0.6
0.8
1.2
1.4
1.6
1.8
2
$\overline{u'v'}/u_{\tau m}^2$